# Capacitively-coupled radio-frequency hydrogen discharges: the role of kinetics

L. Marques[a)]

*Departamento de Física, Universidade do Minho, 4710-057 Braga, Portugal*

J. Jolly

*Laboratoire de Physique et Technologie des Plasmas,*

*Ecole Polytechnique, 91128 Palaiseau Cedex, France*

L. L. Alves[b)]

*Centro de Física dos Plasmas, Instituto Superior Técnico, 1049-001 Lisboa, Portugal*

(Dated: May 3, 2007)

[a)]Also with the Centro de Física dos Plasmas, Instituto Superior Técnico, 1049-001 Lisboa, Portugal

[b)]Electronic mail: llalves@ist.utl.pt

## Abstract

This paper presents a systematic characterization of capacitively-coupled radio-frequency hydrogen discharges, produced within a parallel plate cylindrical setup at different rf applied voltages ($V_{\rm rf} = 50 - 600$ V), frequencies ($f = 13.56 - 40.56$ MHz), and pressures ($p = 0.2 - 1$ torr). A two-dimensional, time-dependent fluid model for charged particle transport is self-consistently solved coupled to a homogeneous kinetic model for hydrogen, including vibrationally excited molecular species and electronically excited atomic species. Numerical simulations are compared with experimental measurements of various plasma parameters. A good quantitative agreement is found between simulations and experiment for the coupled electrical power and the plasma potential. The model underestimates the values of the electron density, the self-bias potential, and the H(n=1) atom density with respect to measurements, but agrees with experiment when predicting that all these parameters increase with either $V_{\rm rf}$, $f$, or $p$. The dissociation degree is about $10^{-3}$ for the work conditions considered. Simulations adopt a wall-recombination probability for H atoms that was experimentally measured, thus accounting for surface modification with discharge operating conditions. Results show the key role played by the atomic wall-recombination mechanism in plasma description.



Keywords: Capacitivel-coupled discharges, radio-frequency discharges, hydrogen plasma, kinetic model, wall-recombination

## I. INTRODUCTION

Capacitively-coupled radio-frequency (ccrf) discharges are currently used in the plasma enhanced chemical vapor deposition of hydrogenated microcrystalline silicon ($\mu$-Si:H) thin films, from a precursor mixture of $SiH_4$-$H_2$, under high dilution conditions for silane.[1–4] The increasing demand for higher throughput, larger processing areas, improved uniformity and film quality, coming from the semiconductor industry, has motivated a special investment in the characterization and optimization of this kind of discharges. In what concerns efficiency, research efforts have concentrated in obtaining higher flows of active neutral and ion species with low energies, as to preserve the quality of surface processing. This challenge was solved either by using discharges operating above the conventional 13.56 MHz frequency[5–20] or by adopting dual frequency sources,[21–28] as to independently control the ion energy and the electron density.

In the case of very-high frequency reactors, it is usual to associate the improvement in the efficiency of plasma-assisted processes with an increase in the density of hydrogen atoms.[29] This is still an open issue, whose investigation can be pursuit by using well-validated simulation models (including a detailed description of the hydrogen kinetic mechanisms) in articulation with experimental diagnostics, particularly for the interaction of atomic species with the wall. This paper investigates pure hydrogen ccrf discharges, produced within a parallel plate cylindrical setup, by comparing numerical simulations with experimental measurements for various plasma parameters, over a broad range of working conditions: $f = 13.56 - 40.56$ MHz frequencies, $p = 0.2 - 1$ torr pressures, and $V_{\rm rf} = 50 - 600$ V applied voltages.

The experimental setup used here is similar to the GEC reference cell and it has been described in detail elsewhere.[30,31] The rf discharge is sustained between parallel plate electrodes (124 mm diameter and 30 mm inter-electrode distance), with the rf voltage applied to the upper electrode through an L-type matching network. A grounded counter-electrode shields the back of the powered electrode, and the plasma is confined to the inter-electrode volume by a cylindrical grid fixed to the counter-electrode. Hydrogen is injected into the reactor at a flow rate of 50 sccm, through a showerhead system set in the upper electrode.

Simulations use a two-dimensional (2D), time-dependent fluid model, describing the production, transport, and destruction of electrons, positive ions $H^+$, $H_2^+$, and $H_3^+$, and negative

ions $H^-$, coupled to a homogeneous kinetic model for hydrogen, including vibrationally excited molecules and electronically excited atoms. Note that a 2D description of the charged particle dynamics is necessary in order to account for asymmetric features in the profiles of density and energy, give correct estimations for the coupled electrical power, and allow the calculation of the self-bias voltage.[32] Calculation results are compared with experimental measurements (and often with earlier predictions, obtained using a simplified kinetic model[32,33]) for the electron density $n_e$, the self-bias voltage $V_{\rm dc}$, the plasma potential $V_p$, the effective electrical power coupled to the plasma $W_{\rm eff}$, and the H atom density $n_{\rm H}$, at various $V_{\rm rf}$, $f$, and $p$. The discussion shows the influence in results of the hydrogen kinetics, focusing on the evolution of the H atoms density with changes in the working conditions.

Usually, fluid-type simulations of ccrf discharges yield electron densities that are systematically underestimated with respect to measurements, yet predicting values for the power coupled to the plasma that agree with experiment.[32–34] The reason for this discrepancy is probably associated with an incomplete description of charge separation regions, as will be also investigated here by comparing measured values and calculation results for the time-average thickness of the rf space-charge sheath.

## II. MODEL DESCRIPTION

The self-consistent modeling of low-temperature non-equilibrium plasmas requires a simultaneous analysis of the charged particle transport and the gas-phase chemistry. This includes the description of collisional interactions between the populations with the plasma-gas system, accounting for the production and destruction of species and/or modifications in their energy distribution. This description focus particularly on the electron population (for which a microscopic analysis is required), as electron-neutral collisions play an essential role in coupling the plasma-gas system and establishing the final gas-phase chemical composition.

In the particular case of hydrogen, a realistic chemistry must include the kinetics of vibrationally excited molecules and of electronically excited atoms. Hydrogen vibrational excited species have an important role in rf discharges, as a significant part of the coupled electrical power is transferred to low-energy vibrational excitations. Moreover, these species are important channels for the production of both atomic hydrogen and charged particles.

To describe pure hydrogen ccrf discharges, we have developed an hybrid calculation code coupling a 2D time-dependent fluid model (accounting for the production, transport and destruction of electrons, positive ions $H^+$, $H_2^+$, and $H_3^+$, and negative ions $H^-$), the two-term homogeneous electron Boltzmann equation [yielding the electron energy distribution function (eedf) in the presence of inelastic and superelastic collisional events, involving both electronically and vibrationally excited states], and a quasi-homogenous collisional-radiative model (crm) for the populations of the H(n=1s,2s,2p,$3-5$) electronically excited atoms and the $H_2(X^1\Sigma_g^+, v = 0-14)$ vibrationally excited ground-state molecules.

### A. Model formulation

The 2D time-dependent fluid model solves the continuity and momentum-transfer equations for electrons and ions, the electron mean energy equation, and Poisson's equation for the rf potential. Boundary conditions involve symmetry considerations at the reactor axis and the imposition, at each physical boundary (electrodes, grid), of electrical conditions for the applied rf potential and of different particle and energy flux conditions. Model calculations are restricted to the volume between the electrodes, corresponding to a 2D workspace delimited by the discharge axis ($r = 0$), the grounded lateral grid ($r = R$), the driven electrode ($z = 0$), and the grounded electrode ($z = d$). Electron transport parameters (etps) are calculated by adopting the local electron mean energy approximation.[32] This assumes that the space-time dependence of the eedf and its related transport parameters (obtained by solving the electron Boltzmann equation) proceeds via the electron mean energy profile, as obtained from the fluid code. We adopt the low-field ion mobilities proposed in Refs. 35–38 ($\mu_{H^+} = 14.6$, $\mu_{H_2^+} = 11.6$, $\mu_{H_3^+} = 10.3$, and $\mu_{H^-} = 43.1$ $V^{-1}$ $s^{-1}$ $cm^2$, values referred to a standard gas density of $2.69 \times 10^{19}$ $cm^{-3}$), with a correction for high reduced-fields (above 50 Td for $H^-$ and 150 Td for the positive ions; 1 Td = $10^{-17}$ V $cm^2$).[32,39,40] A detailed description of the fluid model and of its numerical solution can be found in Refs. 32,33.

The two-term homogeneous electron Boltzmann equation is written by adopting a time-dependent formulation, which accounts for the production of secondary electrons produced in ionizing collisions.[41] As a result, the energy involved in such collisions is distributed among the (primary and secondary) electrons, thus leading to eedfs with less populated tails, which allows to extend Boltzmann calculations of etps up to very-high applied field values

($> 100 - 1000$ Td), or electron mean energies ($> 10 - 20$ eV). This Boltzmann formulation enables the use of the electron mean energy approximation within all the discharge volume, namely inside the highly anisotropic space-charge sheath regions, where the mean energy can reach some very-high values during parts of the rf-cycle. The latter procedure corrects the one adopted in Refs. 32,33 when implementing the electron mean energy approximation, where etps were deduced in an extended energy scale by using a combined Boltzmann-Maxwellian calculation.

Tables I-III summarize the kinetic reactions considered in the model, involving molecular species, atomic species, and charged species, respectively. In these tables, the double arrow ($\longleftrightarrow$) indicates that second-kind collisions are also considered for the reactions where it appears. The cross sections for superelastic collisions are obtained from the ones for the corresponding inelastic processes, by using the Klein-Rosseland's formula.[62] The cross sections for the various electron-neutral collisional processes (appearing in the electron Boltzmann equation) are based on the results of Refs. 42–44. These cross sections were taken up to high-energy values ($\geq 1000$ eV), as to ensure a proper evaluation of the etps in sheath regions, and were normalized in order to yield a good fit between calculated and measured electron transport parameters and rate coefficients for ionization, dissociation and radiative emission.[74,75] Concerning the electronic levels, the results obtained agree with the calculations of Ref. 76 for the excitation of singlet states, and with the theoretical and experimental data available for the excitation of triplet states.[77–79] Notice that the total momentum-transfer cross section includes information about electron collisions with all molecular and atomic species considered, which means that the calculated etps depend on the gas chemical composition. A recent revision of kinetic cross sections for hydrogen was published in Ref. 80.

For the $H_2$ molecule, we consider rotational excitations/de-excitations to/from higher levels (J=3-5), thus ensuring a correct calculation of etps for gas temperatures above 77 K.[81] For the rotational excitations from the J=2-3 levels we adopt the same cross section as for the excitation from J=1, with a threshold correction.[46] As usual,[62] it is assumed that the populations of the rotational excited states follow a Boltzmann distribution, in order to account for superelastic collisions from these levels. The kinetics of vibrational states includes the typical excitation/de-excitation mechanisms due to electron impact collisions (e-V transitions) and heavy species collisions, involving either a vibrational-translational (V-T) or a vibrational-vibrational (V-V) energy transfer. Notice that we consider both direct e-V tran-

sitions (affecting mainly low-energy vibrational levels) and indirect e-V transitions, which proceed through the excitation of electronic singlet states ($B^1\Sigma_u^+$ and $C^1\Pi_u$) by electron impact and subsequent radiative transition to a (high-energy) vibrational level. Dissociation due to e-V, V-V, and V-T mechanisms is also taken into account,[43,50] via the vibrational excitation of (the last) level v=14 to a pseudo-level v=15. For the different excitation, ionization, and dissociation reactions of the $H_2$(v> 0) molecule we adopt the same cross section as for the direct mechanism (from v=0), with a threshold correction.

The H atom kinetics distinguishes between the metastable state H(2s) and the radiative state H(2p) with quantum level n=2, as only the metastable is involved in either the associative ionization or the dissociation reactions (38)-(39) (see Tab. II). For the n=3-5 atomic levels we assume a perfect mixing between their quantum sub-levels. In general, the density of the H atom ground-state is more than 3 orders of magnitude above that of its excited states, and so we usually identify $n_H$ with the H(1s) density. Note that the radiative decay of excited H atoms considers the effects of radiation imprisonment, by using escape factors.[82–85] Note finally that the model uses values for the H atom wall-recombination probability $\gamma_H$ obtained from in-situ laser-induced fluorescence measurements, at various frequencies, pressures, and applied voltages.[65] For the purpose of calculations, a power-law function $\gamma_H = a(f,p)V_{rf}^{b(f)}$ was used to fit the experimental values of the wall-recombination probability, with coefficients $a(f,p)$ and $b(f)$ defined by extrapolating the evolution trends observed at $f = 13.56$ MHz and $p = 0.3$ torr. The fit-curves and the measure-points are shown in Fig. 1, which plots $\gamma_H$ as a function of $V_{rf}$, for various $p$ and $f$.

The crm solves the set of coupled rate balance equations for the 21 neutral (molecular and atomic) species considered. For species $i$ the continuity equation writes

$$\frac{\partial n_i}{\partial t} + \vec{\nabla} \cdot \vec{\Gamma}_i = S_i \quad , \tag{1}$$

where $n_i$ and $\vec{\Gamma}_i \equiv n_i \vec{v}_i$ are the species density and flux, respectively (with $\vec{v}_i$ the corresponding drift velocity); and $S_i \equiv n_i \sum_j k_{ji} n_j + n_i \sum_l k_{li} n_l$ is a source term accounting for the net creation of $i$ (with $k_{ji}$ and $k_{li}$ the rate coefficients for reactions with neutral species $j$ and charged species $l$, respectively).

In order to limit calculation run times (due to the high number of species and kinetic processes considered), we have adopted a quasi-homogenous version of the continuity equa-

tion (1), by averaging it in space as follows

$$\frac{\partial \overline{n_i}}{\partial t} + \frac{2}{R}\Gamma_{r_i}(R,z) + \frac{1}{d}\left[\Gamma_{z_i}(r,d) - \Gamma_{z_i}(r,0)\right] \simeq \sum_j k_{ji}\,\overline{n_i n_j} + \sum_l \overline{k_{li} n_l}\;\overline{n_i} \quad , \tag{2}$$

where the average quantities $\overline{X}$ ($X = n_i, n_i n_j, k_{li} n_l$) are defined as

$$\overline{X} \equiv \frac{2\pi \int_0^d \int_0^R X r dr dz}{\pi R^2 d} \quad . \tag{3}$$

Note that the system of average rate balance equations (2) will be solved for steady-state conditions, meaning that the quantity $\overline{k_{li} n_l}$ represents in fact the *space-time average* of the net production frequency of species $i$, by collisions with charged particles $l$. Moreover, the boundary fluxes in Eq. (2) are set to satisfy the Milne's condition[86]

$$\Gamma_{x_i}|_{\text{wall}} = -D_i \left.\frac{\partial n_i}{\partial x}\right|_{\text{wall}} = \alpha_i\, n_i|_{\text{wall}}\, \frac{v_{\text{th}_i}}{4} \quad (x = r, z) \quad , \tag{4}$$

where, for each species $i$, $D_i$ is the diffusion coefficient ($D_i = 1760/p$ cm$^2$ s$^{-1}$ for H atoms and $D_i = 1160/p$ cm$^2$ s$^{-1}$ for $H_2$ molecules, at 323 K gas temperature), $\alpha_i \equiv \gamma_i/(1 - \gamma_i/2)$ is the wall loss probability, and $v_{\text{th}_i}$ is the thermal velocity.

To calculate the integrals (3) for the average densities $\overline{n_i}$ and $\overline{n_i n_j}$ we distinguish between two plasma regions: a spatially homogeneous one, corresponding to the plasma bulk; a boundary layer, with size equal to the thickness of the plasma sheath, where the densities of neutral species are assumed to decrease linearly. These assumptions correspond to the following density profile

$$n_i(r,z) = n_{b_i} h_i(r) g_i(z) \tag{5a}$$

$$h_i(r) = \begin{cases} 1 & , 0 \le r < R - \delta_R \\ 1 - \dfrac{1 - f_{r_i}}{\delta_R}\,(r - R + \delta_R) & , R - \delta_R \le r \le R \end{cases} \tag{5b}$$

$$g_i(z) = \begin{cases} f_{0_i} + \dfrac{1 - f_{0_i}}{\delta_0} z & , 0 \le z \le \delta_0 \\ 1 & , \delta_0 < z < d - \delta_d \\ 1 - \dfrac{1 - f_{d_i}}{\delta_d}\,(z - d + \delta_d) & , d - \delta_d \le z \le d \end{cases} \quad , \tag{5c}$$

where $n_{b_i}$ is the bulk-density; $\delta_R$, $\delta_0$, and $\delta_d$ are the sheath thicknesses near the grid, the driven electrode, and the grounded electrode, respectively; and the functions $f_{r_i}$, $f_{0_i}$, and $f_{d_i}$ correspond to the ratio of the wall-density to the bulk-density, calculated at $r = R$, $z = 0$,

and $z = d$ using boundary condition (4), i.e.

$$f_{x_i} \equiv \frac{n_i|_{\text{wall}}}{n_{b_i}} = \frac{\dfrac{4}{\alpha_i v_{\text{th}_i}}}{\dfrac{4}{\alpha_i v_{\text{th}_i}} + \dfrac{\delta_x}{D_i}} \quad . \tag{6}$$

As we have associated boundary layers for neutral particles with discharge space-charge sheaths, the quantities $\delta_R$, $\delta_0$, and $\delta_d$ were estimated from the time-average thickness of the regions where the rf field exhibits strong relative gradients. In particular, the sheath edges were taken at positions where the corresponding (axial or radial) reduced electric fields are equal to $\simeq 50$ V cm$^2$.

By using the profile given by Eqs. (5a)-(5c) into Eqs. (2)-(3), the rate balance equation for species $i$ can be rewritten in terms of the bulk-density $n_{b_i}$ as

$$\frac{\partial n_{b_i}}{\partial t} = \left(\frac{\partial n_{b_i}}{\partial t}\right)_{\text{kinetics}} - \left(\frac{\partial n_{b_i}}{\partial t}\right)_{\text{transport}} \quad , \tag{7}$$

where the terms in the right hand-side represent, in order, the net gain rate of $i$ due to the kinetic reactions in the volume, and the net loss rate of $i$ due to transport and wall losses. The quasi-homogenous crm is finally constituted by the set of rate balance equations (7), which are solved coupled to the normalization condition

$$\sum_i n_{b_i} = \frac{p}{k_B T_g} \quad , \tag{8}$$

where $T_g = 323$ K is the gas temperature and $k_B$ is the Boltzmann's constant.

### B. Model solution

The coupling between the different calculation modules follows the usual procedure adopted in the kinetic modeling of such gas discharges.[34,87] The crm runs typically every 5 rf periods, knowing the space-time average values of the charged particle densities and of the rate coefficients for the production/destruction of each neutral species. The crm non-linear equations are solved using a semi-implicit Gauss-Seidel relaxation technique, which searches for the stationary solution $(\partial n_{b_i}/\partial t) \to 0$. Convergence is achieved after several thousand iterations, ensuring relative variations of less than $10^{-12}$ for the density of each neutral species. The new chemical composition of the gas phase, obtained within the crm,

is then used as input data to the homogeneous Boltzmann code, yielding an updated set of electron transport parameters and rate coefficients. The latter is finally used to obtain a self-consistent solution to the charged particle transport model, by adopting the local electron mean energy approximation. The charged particle transport equations are discretized in a $32 \times 16$ ($r$,$z$) point grid by using second-order finite differences, and are solved for typical 1000 time steps within each rf period. In general, a few hundred rf cycles are needed to meet the convergence criterion: relative changes of particle densities, electron mean energy, plasma potential, and self-bias voltage, between two consecutive periods, less than 0.05%.

## III. RESULTS AND DISCUSSION

Figure 2 shows typical axial profiles (at $r = 0$) of the time-average, steady-state charged particle densities, obtained at $V_{\rm rf} = 200$ V, $f = 13.56$ MHz, and $p = 0.3$ torr. Note that: (i) the density profiles exhibit a peak located approximately midway between the two electrodes, as a result of the alternating applied voltage; (ii) the electron density shows very steep gradients in the sheath regions (near the electrodes), associated to the rf electric field confinement; (iii) the dominant ion is $H_3^+$, its maximum density being more than one order of magnitude higher than the mean densities of either $H_2^+$ or $H^+$, due to the very efficient ion conversion reaction (58) of $H_2^+$ into $H_3^+$ (see Tab. III); (iv) the $H^-$ density is smaller than the electron density by about two orders of magnitude, with the negative ions being produced at the sheath edge and remaining confined to a position located midway between the electrodes, where the plasma potential is higher. These ions are mainly created by dissociative attachment (29) from ground-state and from v$= 5 - 8$ vibrationally excited states (see Tab. I), and destroyed by associative detachment by H atoms (57) (see Tab. III).

Figure 3 represents the vibrational distribution function (vdf) of hydrogen molecules at $p = 0.3$ torr, for various rf applied voltages and frequencies. Vibrational excitation proceeds mainly through e-V transitions [see reactions (14)-(16) in Tab. I], directly from ground-state (which is the most important production mechanism of levels v$= 1 - 3$) or indirectly via the $B^1\Sigma_u^+$ and $C^1\Pi_u$ electronic singlet states (for the production of levels v$\geq 3$). Consequently, vibrational excitation is favored by an increase in either $V_{\rm rf}$ or $f$ (as shown in Fig. 3), as both these changes lead to higher electric fields within discharge sheaths (hence, higher effective electrical powers coupled to the plasma), in order to limit the electron displacement and

thus the electron wall losses.[33] The population inversion observed for levels v= $5-7$ comes from the V-T quenching of higher vibrational levels v> 8, which constitutes their most important destruction mechanism. Levels v= 0 and v= $1-8$ are mainly lost by electron impact collisions (14) and wall quenching (32), respectively (see Tab. I).

Figure 4 shows the variation of the time-average electron density with the rf applied voltage, on the axis of the discharge and midway between the two electrodes $n_e(0, d/2)$, at $p = 0.3$ torr and for multiple operating frequencies. For comparison purposes, the simulations presented in this figure were obtained using either the complete kinetic scheme of Tabs. I-III or a simplified kinetic model for hydrogen.[33] The latter considers only reactions (1)-(13), (20)-(21), (44), (46), (48), and (58), which corresponds to neglect the vibrational excitation of hydrogen molecules, and the various kinetic mechanisms accounting for the production / destruction of both H atoms and $H^-$ negative ions. An observation of Fig. 4 reveals that the (complete) kinetic scheme adopted here yields higher electron densities, which is mainly due to the introduction of electron production mechanisms involving H atoms, such as associative ionization (37) and associative detachment (57) (see Tabs. II and III) . These mechanisms become highly competitive with respect to the ionization of (atomic and molecular) hydrogen by electron impact, especially at high-applied voltages and frequencies. Notice that electrons are destroyed mainly by dissociative attachment (29) and by recombination of $H_3^+$ ions (43)-(45) and (50) (see Tabs. I and III). Figure 4 shows also that $n_e$ increases with both $V_{\rm rf}$ and $f$, which comes as a result of the enhanced energy transfer between the rf electric field and the electron plasma population. Figure 4 also compares simulation results with experimental measurements obtained using either a cylindrical Langmuir probe or a planar probe.[34,88] The electron temperature and density were derived from the cylindrical probe characteristics following the techniques described in Refs. 89,90. The planar probe (with 0.25 $cm^2$ surface) received a $-30$ V bias to collect an ion flux. The corresponding electron density was obtained by using Bohm's theory, for a constant 3 eV electron temperature (in coherence with cylindrical probe results). Although a good qualitative agreement is found between simulations and measurements, and despite the fact that the model yields higher electron densities when the complete kinetic scheme is adopted, the calculated values of the electron densities are still below the measured ones by a factor of $1.5-6$, particularly at low applied voltages and frequencies (note that the curves in Fig. 4 were multiplied by a factor of 3).

Figure 5 plots the effective electrical power coupled to the plasma,[32] as a function of the rf applied voltage, at $p = 0.3$ torr and for multiple frequency values. As expected, $W_{\rm eff}$ increases with both $V_{\rm rf}$ and $f$, as a direct result of the higher total voltages $[V_{\rm dc} + V_{\rm rf}\cos(2\pi f t)]$ and currents $[I_{\rm rf}(t)]$ developed in these circumstances. This figure also shows a good agreement between model predictions and experimental measurements for $W_{\rm eff}$, obtained over a large range of working conditions. The experimental results depicted in Fig. 5 were obtained using a subtractive method,[91] which proceeds as follows: (i) for given discharge working conditions we measure the plasma-on generator power input, $P_{\rm on}$, and the rf voltage and current, $V_{\rm rf}$ and $I_{\rm rf}$; (ii) for a plasma-off situation (i.e. by operating the plasma reactor under vacuum conditions), we search for the generator power input, $P_{\rm off}$, that ensures the same $I_{\rm rf}$ value as measured before. Contrarily to classical methods, we use here the rf current (instead of the rf voltage) as calibration parameter; (iii) the effective electrical power coupled to the plasma is given by $W_{\rm eff} = P_{\rm on} - P_{\rm off}$. Note that the matching network is tuned for zero reflected power in both $P_{\rm on}$ and $P_{\rm off}$ measurements.

Figures 6(a) and 6(b) represent, respectively, the time-average plasma potential $V_p$ at position ($r = 0$, $z = d/2$) and the self-bias voltage $V_{\rm dc}$, as a function of the rf applied voltage, at $p = 0.3$ torr and for multiple frequency values. The experimental values of the plasma potential were obtained from the energy distribution function of the $H_3^+$ ions impinging on the grounded electrode, as they perform very few collisions along the bulk-to-wall path. The $H_3^+$ energy distribution function was measured using a mass spectrometer equipped with an energy analyzer.[92] Figures 6(a) and 6(b) show that: (i) $V_p$ varies very little with $f$ being an increasing function of $V_{\rm rf}$; (ii) discharge symmetry (corresponding to smaller $V_{\rm dc}$ absolute values) is favored by a reduction in both $V_{\rm rf}$ and $f$ values; (iii) a good agreement is found between simulation results and experimental measurements for $V_p$, while there is a systematic underestimation of the calculated $V_{\rm dc}$ absolute values with respect to experiment, particularly for high $V_{\rm rf}$. This deviation gives an indication that the model is probably overestimating the ion current at the rf electrode (or, alternatively, that it underestimates the corresponding electron current), thus showing that the fluid description of the rf sheath is not fully achieved.

The latter conclusion is supported by the results in Fig. 4, which reveals a stronger deviation between calculations and measurements of the electron density at low frequencies, hence for discharge conditions characterized by the formation of extended space-charge sheaths.

Again, there is the possibility that the observed disagreement is associated to an incomplete description of the discharge sheaths, for example due to the absence of the nonlinear inertia term in the electron flux equation.[32] However, the fact remains that even with this limitation the model gives good predictions for the effective electrical power coupled to the plasma, at various rf applied voltages, frequencies, and pressures (see Figs. 5 and 9). In an attempt to explain these (apparently) contradictory results, Fig. 7 plots the average thickness $\delta$ of a mean space-charge sheath, as a function of the average sheath voltage $V_{\rm sh}$, at $p = 0.5$ torr and for multiple frequency values. The results depicted in this figure were obtained: (i) from simulations using the complete model developed here, by calculating single mean values of $\delta$ and $V_{\rm sh}$ as representative of the (asymmetric) space-charge regions with the electrodes (as before, the values of $\delta$ were estimated from the profiles of the corresponding rf electric field); (ii) semi-empirically, using a simplified electric description of the discharge combined with electrical measurements of the plasma reactance $X_p$.[93] The latter is written for a symmetric discharge, by considering the contribution of both the inductance of the plasma bulk,[94] $L_b = R_b/\nu_{\rm eff}$ (where $R_b$ is the bulk resistance and $\nu_{\rm eff}$ is an effective electron-neutral collision frequency), and the reactance of the plasma sheath,[94] $X_{\rm sh} = -1/(C_{\rm sh}\omega)$ [where $\omega = 2\pi f$ and $C_{\rm sh} = \varepsilon_0 A/(2\delta)$ is the capacitance of the plasma sheaths, with $\varepsilon_0$ the vacuum permittivity and $A$ the boundary surface], yielding

$$\delta = \frac{\varepsilon_0 \omega A}{2}\left(\frac{\omega}{\nu_{\rm eff}} R_b - X_p\right) \quad . \tag{9}$$

Notice that the bulk inductance has a non negligible effect upon the plasma reactance at frequencies higher than the conventional 13.56 MHz value, as experimentally observed by several authors.[95,96] Electrical measurements also show that the resistances of the plasma bulk and sheath exhibit variations with the rf current according to the power laws $R_b \propto I_{\rm rf}^{-1}$ and $R_{\rm sh} \propto I_{\rm rf}^{0.5}$,[93] thus yielding an effective (total) power coupled to the plasma that satisfies

$$W_{\rm eff} = W_b + W_{\rm sh} \tag{10a}$$

$$W_b = \frac{1}{2} R_b I_{\rm rf}^2 \propto I_{\rm rf} \tag{10b}$$

$$W_{\rm sh} = \frac{1}{2} R_{\rm sh} I_{\rm rf}^2 \propto I_{\rm rf}^{2.5} \quad . \tag{10c}$$

The simulation results presented in Fig. 7 predict a very small increase of $\delta$ with $V_{\rm sh}$, in accordance with the Child-Langmuir law.[94] However, model predictions are above measured values, although the deviation reduces as the frequency increases. This is coherent with the

disagreement observed between calculations and measurements of the electron density (see Fig. 4), for a similar $W_{\rm eff}$ value. In fact, the product $\delta n_e$ relates to the displacement current flowing through the plasma sheaths, being approximately constant for given rf current [hence for given coupled power, see Eqs. (10)], according to[94] ($e$ is the electron charge)

$$I_{\rm rf} \sim e\delta n_e \omega A \quad . \tag{11}$$

Incidentally, the previous analysis also explains the quality of predictions for $n_e$ given by homogeneous *global models*,[93,94,97–103] as they strongly underestimate the thickness of space-charge sheaths.[93]

From the relationship between the rf current and voltage[94]

$$I_{\rm rf} \simeq C_{\rm sh}\frac{dV_{\rm sh}}{dt} \sim \frac{\varepsilon_0 A}{2\delta}\omega V_{\rm rf} \quad , \tag{12}$$

one concludes that an increase in $\delta$ is associated to a decrease in $I_{\rm rf}$ (hence in $W_{\rm eff}$) for given $V_{\rm rf}$. This is now coherent with the fact that simulations yield a small underestimation of $W_{\rm eff}$ with respect to experiment (see Fig. 5), which reduces as the frequency increases (see Fig. 7) or the rf applied voltage decreases [in which case $I_{\rm rf}$ also decreases and $W_{\rm eff} \simeq W_b$, see Eqs. (10), meaning that the electrical power is mostly coupled to the plasma bulk under these conditions]. The latter analysis was previously confirmed, by comparing calculations and measurements for the ($I_{\rm rf}$, $V_{\rm rf}$) discharge characteristic, at various frequencies.[104]

Figure 8 plots, as a function of the rf applied voltage, the time-average density of H atoms $n_{\rm H}$ [and the dissociation degree $n_{\rm H}/(n_{\rm H} + 2n_{\rm H_2})$], on the axis of the discharge at 12 mm from the driven electrode, at $p = 0.5$ torr and for multiple frequencies. The production of atomic species proceeds mainly via electron collisions [especially for the H(1s,2s,2p,3) atomic states; see reactions (22)-(28) in Tab. I], which explains the increase in the dissociation of hydrogen with either the rf applied potential or the excitation frequency (see also Fig. 4). Notice that the dissociation by collisions with $H_2$ molecules [reactions (39)-(40) in Tab. II] is also an important production mechanism for the H(2s,2p) states, whereas the main destruction channels of H atoms are (see Tab. II) radiative decay (35) for H(2p,$3-5$), associative ionization (37) for H(2s), quenching with $H_2$ molecules (39)-(40) for H(2s,2p), and wall recombination (42) for ground state H(1s). Figure 8 also compares simulation results with experimental measurements of the absolute H atom density, obtained by two-photon absorption laser-induced fluorescence (TALIF) diagnostics,[65] using the known Kr:H

detection sensitivity ratio.[105] Notice the good qualitative agreement between simulations and experiment, although the calculated values of $n_{\rm H}$ are below the measured ones (note that the curves in Fig. 8 were multiplied by a factor of 4), following the discrepancy already observed for the electron density (see Fig. 4).

We now study the evolution of results with pressure, starting with the plot of $W_{\rm eff}$ vs. $p$ at $V_{\rm rf} = 100$ V and for multiple frequencies (see Fig. 9). As before, a good agreement is found between model predictions and experimental measurements for the electrical power coupled, over a large range of discharge operating conditions. Figure 9 shows that $W_{\rm eff}$ increases with $p$, for pressures up to 1 torr. This increase is associated to the enhancement of the rf electric field within discharge sheaths, induced by the compression of these charge separation regions.

Figure 10 shows the variation of the time-average electron density with pressure, on the axis of the discharge and midway between the two electrodes $n_e(0, d/2)$, at $V_{\rm rf} = 100$ V and for various frequencies. The simulations presented in this figure were obtained using either the complete kinetic scheme of Tabs. I-III or the simplified kinetic model previously mentioned (where H atoms are not considered).[33] The experimental values reported were obtained either by Langmuir probe measurements[34,88] or semi-empirically, using a simplified electric description of the discharge combined with electrical measurements of the plasma bulk resistance $R_b$. The latter can be written as[94] $R_b = \nu_{\rm eff} L_b = \nu_{\rm eff}/(\omega_p^2 C_0)$ (where $\omega_p = \sqrt{n_e e^2/m_e \varepsilon_0}$ is the electron plasma frequency, with $m_e$ the electron mass, and $C_0 = \varepsilon_0 A/d$ is the capacitance of the reactor), from which it is possible to deduce the electron density

$$n_e = \frac{m_e \nu_{\rm eff}}{e^2} \frac{d}{A} \frac{1}{R_b} \quad . \tag{13}$$

Results confirm that the extra reactions included in the complete hydrogen kinetics do lead to higher electron densities (see also Fig. 4), further showing that this effect is enhanced with pressure increase. This behavior is mainly due to electron production mechanisms involving H atoms, such as associative ionization (AI) and associative detachment (AD) [see reactions (37) and (57) in Tabs. II-III], whose relative importance increases with pressure. In fact, although the electron production rates via AI and AD, at position $(0, d/2)$, present a limited variation (of less than a factor of 2 for AI and of less than a factor of 30 for AD), over the pressure range considered here, the ionization rate of (atomic and molecular) hydrogen by electron impact becomes highly attenuated at $(0, d/2)$, being strongly enhanced

within discharges sheaths, due to the decrease in $V_p$ as $p$ increases. However, even with this improvement, the calculated values of the electron density are still below the measured ones by a factor of 1.5-5 (note that the curves in Fig. 9 were multiplied by a factor of 4). Moreover, Fig. 10 evidences also a qualitative disagreement between simulations and Langmuir probe measurements (that show negligible variations of $n_e$ with $p$), which is not confirmed neither by electrical measurements nor by *plasma transmission probe* diagnostics[93,106] (that show a clear increase of $n_e$ with $p$).

To further investigate this question Fig. 11 plots, as a function of pressure, the time-average density of H atoms (and the dissociation degree), on the axis of the discharge at 12 mm from the driven electrode, at $W_{\text{eff}} = 30$ W and for different frequencies. The simulation results presented in this figure were obtained either with the H atom wall-recombination probability $\gamma_{\text{H}}$ shown in Fig. 1 (as obtained from in-situ measurements), or by taking a constant value $\gamma_{\text{H}} = 10^{-2}$ as for an aluminum driven electrode.[65] As before (see Fig. 8), the experimental measurements reported here are found above simulation results (note that the curves in Fig. 11 were multiplied by a factor of 3). Notice that model results, obtained with in-situ measured $\gamma_{\text{H}}$ values, reproduce the experimental increase of $n_{\text{H}}$ with $p$, in accordance with the electron density variation (see Fig. 10). Notice also that the latter evolution of $n_{\text{H}}$ is not attained in simulations at constant $\gamma_{\text{H}} = 10^{-2}$, which demonstrates the key role played by the atomic wall-recombination mechanism in plasma description.

## IV. SUMMARY

This paper has studied capacitively-coupled radio-frequency hydrogen discharges, produced within a parallel plate cylindrical setup at different rf applied voltages ($V_{\text{rf}} = 50 - 600$ V), frequencies ($f = 13.56 - 40.56$ MHz), and pressures ($p = 0.2 - 1$ torr). A two-dimensional, time-dependent fluid model, describing the production, transport, and destruction of electrons, positive ions $H^+$, $H_2^+$, and $H_3^+$, and negative ions $H^-$, was self-consistently solved coupled to a homogeneous kinetic model for hydrogen, including $H_2(X^1\Sigma_g^+, v = 0-14)$ vibrationally excited ground-state molecules and H(n=1s,2s,2p,3 − 5) electronically excited atoms. The inclusion of this kinetic model led to higher electron densities, due to the presence of electron production mechanisms involving H atoms, such as associative ionization and associative detachment. The model adopted a wall-recombination probability for H

atoms, obtained from in-situ measurements at various $V_{\mathrm{rf}}$, $f$, and $p$.

Numerical simulations were compared with experimental measurements of various plasma parameters. A good quantitative agreement was found between simulations and experiment for the coupled electrical power and the plasma potential, at various applied voltages, frequencies, and pressures. However, the model has generally underestimated the electron density and the self-bias potential with respect to measured values, which probably indicates that the fluid description of rf space-charge sheaths is still incomplete. This analysis is coherent with the following facts: (i) model predictions for the space-charge sheath thickness $\delta$ are above measurements; (ii) the electron density is inversely proportional to $\delta$ for given coupled electrical power (or for given rf current).

Simulation results showed that both the electron density $n_e$ and the H(n=1) atom density $n_{\mathrm{H}}$ increase with the rf applied voltage, frequency, and pressure, thus confirming that the production of atomic species proceeds mainly via electron collisions. These results were found in qualitative agreement with Langmuir probe measurements (for the evolution of $n_e$ with $V_{\mathrm{rf}}$ and $f$), electric and plasma transmission probe measurements (for the evolution of $n_e$ with $p$), and TALIF measurements (for the evolution of $n_{\mathrm{H}}$ with $V_{\mathrm{rf}}$, $f$, and $p$). A disagreement was observed between simulations and Langmuir probe measurements for the electron density at various pressures (showing negligible variations of $n_{\mathrm{H}}$ with $p$), which is probably due to uncertainties with this diagnostic. The dissociation degree was about $10^{-3}$ for the work conditions considered. The quality of simulations was strongly related to the use of a wall-recombination probability for H atoms that was experimentally measured, thus accounting for surface modification with discharge operating conditions. Results evidenced the key role played by the atomic wall-recombination mechanism in plasma description.

[1] E. Vallat-Sauvain, U. Kroll, J. Meier, N. Wyrsch, and A. Shah, J. Non-Cryst. Solids **266-269**, 125 (2000).

[2] E. Vallat-Sauvain, U. Kroll, J. Meier, A. Shah, and J. Pohl, J. Appl. Phys. **87**, 3137 (2000).

[3] P. Roca i Cabarrocas, J. Non-Cryst. Solids **266-269**, 31 (2000).

[4] M. Kondo, M. Fukawa, L. Gou, and A. Matsuda, J. Non-Cryst. Solids **266-269**, 84 (2000).

[5] H. Curtins, N.Wyrsch, M. Favre, and A. V. Shah, Plasma Chem. Plasma Proc. **7**, 267 (1987).

[6] M. Surendra and D. B. Graves, Appl. Phys. Lett. **59**, 2091 (1991).

[7] F. Finger, U. Kroll, V. Viret, A. V. Shah, W. Beyer, X.-M. Tang, J. Weber, A. A. Howling, and C. Hollenstein, J. Appl. Phys. **71**, 5665 (1992).

[8] A. A. Howling, J. L. Dorier, C. Hollenstein, U. Kroll, and F. Finger, J. Vac. Sci. Technol. A **10**, 1080 (1992).

[9] M. Heintze, R. Zedlitz, and G. H Bauer, J. Phys. D **26**, 1781 (1993).

[10] V. Vahedi, C. K. Birdsall, M. A. Lieberman, G. DiPeso, and T. D. Rognlien, Phys. Fluids B **5**, 2719 (1993).

[11] F. Finger, P. Hapke, M. Luysberg, R. Carius, H. Wagner, and M. Scheib, Appl. Phys. Lett. **65**, 2588 (1994).

[12] M. J. Colgan, M. Mayyappan, and D. E. Murnick, Plasma Sources Sci. Technol. **3**, 181 (1994).

[13] H. Meiling, J. F. M. Westendorp, J. Hautala, Z. Saleh, and C. T. Malone, Mat. Res. Soc. Symp. Proc. **345**, 65 (1994).

[14] J. F. M. Westendorp, H. Meiling, J. D. Pollock, D. W. Berrian, A. H. Laflamme, J. Hautala, and J. Vanderpot, Mat. Res. Soc. Symp. Proc. **345**, 65 (1994).

[15] H. Keppner, U. Kroll, J. Meier, and A. V. Shah, Solid State Phenomena **44**, 97 (1995).

[16] J. Hautala, Z. Saleh, J. F. M. Westendorp, S. Sherman, and S. Wagner, Mat. Res. Soc. Symp. Proc. **420**, 83 (1996).

[17] M. Meyyappan and M. J. Colgan, J. Vac. Sci. Technol. A **14**, 2790 (1996).

[18] T. Kitajima, Y. Takeo, N. Nakano, and T. Makabe, J. Appl. Phys. **84**, 5928 (1998).

[19] E. Amanatides and D. Mataras, J. Appl. Phys. **89**, 1556 (2001).

[20] M. Fukawa, S. Suzuki, L. Guo, M. Kondo, and A. Matsuda, Solar Energy Materials & Solar Cells **66**, 217 (2001).

[21] H. H. Goto, H.-D. Lowe, and T. Ohmi, J. Vac. Sci. Technol. A **10**, 3048 (1992).

[22] H. H. Goto, H.-D. Lowe, and T. Ohmi, IEEE Trans. Semiconductor Manufacturing **6**, 58 (1993).

[23] W. Tsai, G. Mueller, R. Lindquist, B. Frazier, and V. Vahedi, J. Vac. Sci. Technol. B **14**, 3276 (1996).

[24] H. C. Kim and V. I. Manousiouthakis, J. Vac. Sci. Technol. A **16**, 2162 (1998).

[25] T. Kitajima, Y. Takeo, and T. Makabe, J. Vac. Sci. Technol. A **17**, 2510 (1999).

[26] S. Rauf and M. J. Kushner, IEEE Trans. Plasma Sci. **27**, 1329 (1999).

[27] T. Kitajima, Y. Takeo, Z. L. Petrovic, and T. Makabe, Appl. Phys. Lett. **77**, 489 (2000).

[28] J. Robiche, P. C. Boyle, M. M. Turner, and A. R. Ellingboe, J. Phys. D **36**, 1810 (2003).

[29] U. Kroll, J. Meier, P. Torres, J. Pohl, and A. Shah, J. Non-Cryst. Solids **227-230**, 68 (1998).

[30] M. Hertl, J. Jolly, and G. Baravian, J. Appl. Phys. **92**, 710 (2002).

[31] O. Leroy, G. Gousset, L. L. Alves, J. Perrin, and J. Jolly, Plasma Sources Sci. Technol. **7**, 348 (1998).

[32] A. Salabas, G. Gousset, and L. L. Alves, Plasma Sources Sci. Technol. **11**, 448 (2002).

[33] A. Salabas, L. Marques, J. Jolly, G. Gousset, and L. L. Alves, J. Appl. Phys. **95**, 4605 (2004).

[34] L. Marques, J. Jolly, G. Gousset, and L. L. Alves, J. High Temp. Mater. Processes **8**, 499 (2004).

[35] A. V. Phelps, J. Phys. Chem. Ref. Data **19**, 653 (1990).

[36] J. Bretagne, G. Gousset, and T. Simko, J. Phys. D **27**, 1866 (1994).

[37] T. Simko, M. Martisovits, J. Bretagne, and G. Gousset, Phys. Rev. E **56**, 5908 (1997).

[38] H. Ellis, R. Pai, E. McDaniel, E. Mason, and L. Viehland, Atomic Data and Nuclear Data Tables **17**, 178 (1976).

[39] E. W. McDaniel and E. A Mason, *The Mobility and Diffusion of Ions in Gases* (John Wiley, New York, 1973).

[40] A. Ward, J. Appl. Phys. **33**, 2789 (1962).

[41] S. Yoshida, A. V. Phelps, and L. C. Pitchford, Phys. Rev. A **27**, 2858 (1983).

[42] A. V. Phelps et al, ftp://jila.colorado.edu/collision_data/electronneutral/electron.txt (1997).

[43] J. Loureiro and C. M. Ferreira, J. Phys. D **22**, 1680 (1989).

[44] H. Tawara, Y. Itikawa, H. Nishimura, and M. Yoshino, J. Phys. Chem. Ref. Data **19**, 617 (1990).

[45] B. Wingerden, E. Weigold, F. de Heer, and K. J. Nygaard, J. Phys. B **10**, 1345 (1977).

[46] E. Gerjuoy and S. Stein, Phys. Rev. **98**, 1848 (1955).

[47] H. Nishimura, A. Danjo, and H. Sugahara, J. Phys. Soc. Jpn **54**, 1757 (1985).

[48] J. R. Hiskes, J. Appl. Phys. **70**, 3409 (1991).

[49] B. Gordiets, S. Mamedov, and L. Shelepin, Sov. Phys. - JETP **40**, 640 (1975).

[50] M. Cacciatore, M. Capitelli, and M. Dilonardo, Chem. Phys. **34**, 193 (1978).

[51] C. Gorse, M. Capitelli, M. Bacal, J. Bretagne, and A. Laganà, Chem. Phys. **117**, 177 (1987).

[52] D. Rapp and P. Englander-Golden, J. Chem. Phys. **43**, 1464 (1965).

[53] D. Rapp, P. Englander-Golden, and D. Briglia, J. Chem. Phys. **42**, 4081 (1965).

[54] T. Fujimoto, K. Sawada, and K. Takahata, J. Appl. Phys. **66**, 2315 (1989).

[55] B. P. Lavrov, Opt. Spectrosc. **42**, 250 (1977).

[56] A. P. Hickman, Phys. Rev. A **43**, 3495 (1991).

[57] K. Hassouni, A. Gicquel, M. Capitelli, and J. Loureiro, Plasma Sources Sci. Technol. **8**, 494 (1999).

[58] C. Gorse, M. Capitelli, J. Bretagne, and M. Bacal, Chem. Phys. **93**, 1 (1985).

[59] M. Mukherjee, M. Basu, and A. Gosh, Phys. Rev. A **36**, 937 (1987).

[60] I. Bray, D. A. Konovalov, and I. E. McCarthy, Phys. Rev. A **43**, 5874 (1991).

[61] H. Drawin, Rapport EUR-CEA-FC-383, Euratom-CEA (1967).

[62] I. I. Sobelman, L. A. Vainshtein, and E. A. Yukov, *Excitation of Atoms and Broadening of Spectral Lines* (Springer, Berlin, 1980).

[63] M. Glass-Maujean, Phys. Rev. Lett. **62**, 144 (1989).

[64] N. Terazawa, M. Ukai, N. Kouchi, K. Kameta, and Y. Hatano, J. Chem. Phys **99**, 1637 (1993).

[65] J. Jolly and J.-P. Booth, J. Appl. Phys. **97**, 103305 (2005).

[66] R. K. Janev, W. D. Langer, K. Evans, and D. E. Post, *Elementary processes in hydrogen - helium plasmas: cross sections and reaction rate coefficients*, edited by G. Ecker, P. Lambropolous, and H. Wlather (Springer, Berlin, 1987).

[67] A. A. Matveyev and V. P. Silakov, Plasma Sources Sci. Technol. **4**, 606 (1995).

[68] O. Bely and S. B. Schwartz, J. Phys. B **2**, 159 (1969).

[69] M. J. J. Eerden, M. C. M. van de Sanden, D. K. Otorbaev, and D. C. Schram, Phys. Rev. A **51**, 3362 (1995).

[70] A. Dalgarno and J. C. Browne, Astrophys. J. **149**, 231 (1967).

[71] M. T. Bowers, D. D. Elleman, and J. King, J. Chem. Phys. **50**, 4787 (1969).

[72] L. P. Theard and W. T. Huntress Jr., J. Chem. Phys. **60**, 2840 (1974).

[73] M. J. Kushner, J. Appl. Phys. **63**, 2532 (1988).

[74] J. Dutton, J. Phys. Chem. Ref. Data **4**, 577 (1975).

[75] A. V. Phelps et al, ftp://jila.colorado.edu/collision_data/electronneutral/eletrans.txt (1998).

[76] R. Celiberto and T. N. Rescigno, Phys. Rev. A **47**, 1939 (1993).

[77] S. Corrigan, J. Chem. Phys. **43**, 4381 (1965).

[78] S. Chung, C. C. Lin, and E. Lee, Phys. Rev. A **12**, 1340 (1975).

[79] H. Nishimura and A. Danjo, J. Phys. Soc. Jpn **55**, 3031 (1986).

[80] M. Capitelli, R. Celiberto, F. Esposito, A. Laricchiuta, K. Hassouni, and S. Longo, Plasma Sources Sci. Technol. **11**, 7 (2002).

[81] A. G. Engelhardt and A. V. Phelps, Phys. Rev. **131**, 2115 (1963).

[82] T. Holstein, Phys. Rev. **72**, 1212 (1947).

[83] T. Holstein, Phys. Rev. **83**, 1159 (1951).

[84] P. J. Walsh, Phys. Rev. **116**, 511 (1959).

[85] J. W. Mills and G. M. Hieftje, Spectrochim. Acta **39B**, 859 (1984).

[86] E. W. McDaniel, *Collision Phenomena in Ionized in Gases* (John Wiley, New York, 1964).

[87] P. Diomede, M. Capitelli, and S. Longo, Plasma Sources Sci. Technol. **14**, 459 (2005).

[88] L. Marques, A. Salabas, G. Gousset, J. Jolly, and L. L. Alves, *Proceedings of the 16*$^{\text{th}}$ *European Sectional Conference on the Atomic and Molecular Physics of Ionized Gases and 5*$^{\text{th}}$ *International Conference on Reactive Plasmas*, edited by N. Sadeghi and H. Sugai (Grenoble, France, 2002) p. 69.

[89] Z. Zakrzewski and T. Kopiczynski, Plasma Phys. **16**, 1195 (1974).

[90] M. Tichy, M. Sicha, P. David, and T. David, Contrib. Plasma Phys. **34**, 59 (1994).

[91] V. A. Godyak and R. B. Piejak, J. Vac. Sci. Technol. A **8**, 3833 (1990).

[92] K. Köhler, J. W. Coburn, D. E. Horne, E. Kay, and J. H. Keller, J. Appl. Phys. **57**, 59 (1985).

[93] S. Dine, Ph.D Thesis (Paris XI University, Paris, 2006).

[94] M. A. Lieberman and A. J. Lichtenberg, *Principles of Plasma Discharges and Materials Processing* (John Wiley, New York, 1994).

[95] J. Taillet, American Journal of Physics **37**, 423 (1969).

[96] K. E. Orlov and A. S. Smirnov, Plasma Sources Sci. Technol. **10**, 541 (2001).

[97] G. R. Misium, A. J. Lichtenberg, and M. A. Lieberman, J. Vac. Sci. Technol. A **7**, 1007 (1989).

[98] C. Lee and M. A. Lieberman, J. Vac. Sci. Technol. A **13**, 368 (1995).

[99] Y. T. Lee, M. A. Lieberman, A. J. Lichtenberg, F. Bose, H. Baltes, and R. Patrick, J. Vac. Sci. Technol. A **15**, 113 (1997).

[100] T. Kimura and K. Ohe, Plasma Sources Sci. Technol. **8**, 553 (1999).

[101] T. H. Chung, H. J. Yoon, and D. C. Seo, J. Appl. Phys. **86**, 3536 (1999).

[102] J. T. Gudmundsson, Plasma Sources Sci. Technol. **10**, 76 (2001).

[103] T. Kimura, A. J. Lichtenberg, and M. A. Lieberman, Plasma Sources Sci. Technol. **10**, 430 (2001).

[104] L. S. A. Marques, J. Jolly, and L. L. Alves, Plasma Process. Polym. (in press, 2007).

[105] M. G. H. Boogaarts, S. Mazouffre, G. J. Brinkman, H. W. P. van der Heijden, P. Vankan, J. A. M. van der Mullen, D. C. Schram, and H. F. Döbele, Rev. Sci. Instrum. **73**, 73 (2002).

[106] S. Dine, J.-B. Booth, G. Curley, C. Corr, J. Jolly, and J. Guillon, Plasma Sources Sci. Technol. **14**, 777 (2005).

TABLE I: Hydrogen kinetic reactions for molecular species.

| **Nb.** | **Coll. type** | | **Reaction** | | **Refs.** |
|---|---|---|---|---|---|
| (1)$^\star$ | Elastic | e + $H_2$(v) | $\longrightarrow$ | e + $H_2$(v) | 42–45 |
| (2)$^\star$ | Electronic | e + $H_2$(v) | $\longrightarrow$ | e + $H_2(b^3\Sigma_u^+)$ | 43,44 |
| (3)$^\star$ | excitation | | $\longrightarrow$ | e + $H_2(c^3\Pi_u)$ | 43,44 |
| (4)$^\star$ | of triplet states | | $\longrightarrow$ | e + $H_2(a^3\Sigma_g^+)$ | 43,44 |
| (5)$^\star$ | | | $\longrightarrow$ | e + $H_2(e^3\Sigma_u^+)$ | 43,44 |
| (6)$^\star$ | Electronic | e + $H_2$(v) | $\longrightarrow$ | e + $H_2(B^1\Sigma_u^+)$ | 43,44 |
| (7)$^\star$ | excitation | | $\longrightarrow$ | e + $H_2(C^1\Pi_u)$ | 43,44 |
| (8)$^\star$ | of singlet states | | $\longrightarrow$ | e + $H_2(E^1\Sigma_g^+$ - $F^1\Sigma_g^+)$ | 43,44 |
| (9)$^\star$ | | | $\longrightarrow$ | e + $H_2(B'^1\Sigma_u^+)$ | 43,44 |
| (10)$^\star$ | | | $\longrightarrow$ | e + $H_2(D^1\Pi_u)$ | 43,44 |
| (11)$^\star$ | | | $\longrightarrow$ | e + $H_2(B''^1\Sigma_u^+)$ | 43,44 |
| (12)$^\star$ | | | $\longrightarrow$ | e + $H_2(D'^1\Pi_u)$ | 43,44 |
| (13)$^\star$ | Rot. exc. | e + $H_2$(v,J=0-3) | $\longleftrightarrow$ | e + $H_2$(v,J+2) | 42–44,46 |
| (14)$^\star$ | Vib. exc.[a] | e + $H_2$(v) | $\longleftrightarrow$ | e + $H_2$(v+i), i=1-3 | 42–44,47 |
| (15)$^\star$ | | e + $H_2(B^1\Sigma_u^+)$ | $\xrightarrow{1.00}$[b] | e + $H_2$(v') | 43,44,48 |
| (16)$^\star$ | | e + $H_2(C^1\Pi_u)$ | $\xrightarrow{1.00}$[b] | e + $H_2$(v') | 43,44,48 |
| (17) | | $H_2$(v) + $H_2$(w) | $\longleftrightarrow$ | $H_2$(v-1) + $H_2$(w+1) | 43,49,50 |
| (18) | | $H_2$(v) + $H_2$(w) | $\longleftrightarrow$ | $H_2$(v+1) + $H_2$(w) | 43,49,50 |
| (19) | | $H_2$(v) + H(1s) | $\longleftrightarrow$ | $H_2$(v+i) + H(1s), i=1-5 | 43,51 |
| (20)$^\star$ | Ionization | e + $H_2$(v) | $\xrightarrow{0.93}$[c] | 2e + $H_2^+$ | 37,43,44,51–53 |
| (21)$^\star$ | by el. impact | | $\xrightarrow{0.07}$[c] | 2e + $H^+$ + H(1s) | 37,43,44,51–53 |

TABLE I: Hydrogen kinetic reactions for molecular species (cont).

| **Nb.** | **Coll. type** | | **Reaction** | | **Refs.** |
|---|---|---|---|---|---|
| (22)$^\star$ | Dissociation | e + $H_2(b^3\Sigma_u^+)$ | $\overset{1.000^d}{\longrightarrow}$ | e + 2H(1s) | 43,44 |
| (23)$^\star$ | by el. impact | e + $H_2(c^3\Pi_u)$ | $\overset{1.000^d}{\longrightarrow}$ | e + 2H(1s) | 43,44 |
| (24)$^\star$ | | e + $H_2(a^3\Sigma_g^+)$ | $\overset{1.000^d}{\longrightarrow}$ | e + 2H(1s) | 43,44 |
| (25)$^\star$ | | e + $H_2(e^3\Sigma_u^+)$ | $\overset{1.000^d}{\longrightarrow}$ | e + 2H(1s) | 43,44 |
| (26)$^\star$ | | e + $H_2(D^1\Pi_u)$ | $\overset{0.298^d}{\longrightarrow}$ | e + H(1s) + H(n=2s,2p,3) | 54,55 |
| (27)$^\star$ | | e + $H_2(B"^1\Sigma_u^+)$ | $\overset{0.967^d}{\longrightarrow}$ | e + H(1s) + H(n=2s,2p,3) | 54,55 |
| (28)$^\star$ | | e + $H_2(D'^1\Pi_u)$ | $\overset{0.579^d}{\longrightarrow}$ | e + H(1s) + H(n=2s,2p,3) | 54,55 |
| (29)$^\star$ | Diss. attach. | e + $H_2$(v=0-9) | $\longrightarrow$ | $H_2^- \longrightarrow$ H(1s) + $H^-$ | 56 |
| (30) | Dissociation | $H_2$(v=14) + $H_2$(w) | $\longleftrightarrow$ | 2H(1s) + $H_2$(w) | 57 |
| (31) | by vib. pump. | $H_2$(v=14) + H(1s) | $\longleftrightarrow$ | 3H(1s) | 57 |
| (32) | Wall quench. | $H_2$(v> 0) + wall | $\overset{\gamma_{H_2(v>0)}=0.07^e}{\longrightarrow}$ | $H_2$(v=0) | 58 |

$^\star$ Rate coefficient calculated by integrating the corresponding cross section over the eedf.

[a]Second-kind collisions considered only for superelastic transitions to ground-state.

[b]Branching ratio for e-V excitations via electronic singlet states.

[c]Branching ratio for ionization by electron impact, from Refs. 37,44.

[d]Branching ratio for molecular dissociation by electron impact, obtained from emission cross sections.[54]

[e]Wall de-excitation probability for the $H_2$ molecule.

TABLE II: Hydrogen kinetic reactions for atomic species.

| **Nb.** | **Coll. type** | | **Reaction** | | **Refs.** |
|---|---|---|---|---|---|
| (33)$^\star$ | Elastic | e + H(n) | $\longrightarrow$ | e + H(n) | 59,60 |
| (34)$^\star$ | Elec. excitation | e + H(n) | $\longleftrightarrow$ | e + H(n') | 61 |
| (35) | Radiative decay | H(n) | $\longrightarrow$ | H(n') + h$\nu$ | 62 |
| (36)$^\star$ | Elec. ionization | 2e + H(n) | $\longrightarrow$ | e + $H^+$ | 61 |
| (37) | Assoc. ionization | H(2s)+ $H_2$(v) | $\longrightarrow$ | e + $H_3^+$ | 63 |
| (38) | Dissociation | H(2s) + $H_2$(v) | $\longrightarrow$ | 3H(1s) | 63 |
| (39) | Quenching | H(2s) + $H_2$(v) | $\longrightarrow$ | H(2p) + $H_2$(v) | 64 |
| (40) | with $H_2$ | H(2p) + $H_2$(v) | $\longrightarrow$ | H(2s) + $H_2$(v) | 64 |
| (41) | Wall quench. | H(n>1s) + wall | $\xrightarrow{\gamma_{H(n>1)}=1.0^f}$ | H(1s) | |
| (42) | Wall recombination | H(1s) + wall | $\xrightarrow{\gamma_H{}^g}$ | 1/2 $H_2$(v=0) | 65 |

$^\star$ Rate coefficient calculated by integrating the corresponding cross section over the eedf.

$^f$Wall de-excitation probability for H atoms.

$^g$Wall-recombination probability for H atoms, from in-situ measurements.[65]

TABLE III: Hydrogen kinetic reactions for charged species.

| **Nb.** | **Coll. type** | | **Reaction** | | **Refs.** |
|---|---|---|---|---|---|
| (43)$^\star$ | Electron-ion | $e + H_3^+$ | $\xrightarrow{0.72}$ | 3H(1s) | 66 |
| (44)$^\star$ | recombination | | $\xrightarrow{0.28}$ | $H_2$(v>5) + H(2s,2p) | 66 |
| (45) | | $2e + H_3^+$ | $\longrightarrow$ | $e + H_2(X^1\Sigma_g^+) + H(1s)$ | 67 |
| (46)$^\star$ | | $e + H_2^+$ | $\longrightarrow$ | H(1s) + H(n>1s) | 66 |
| (47) | | $2e + H_2^+$ | $\longrightarrow$ | e + 2H(1s) | 67 |
| (48) | | $e + H^+$ | $\longrightarrow$ | H(n) + h$\nu$ | 66 |
| (49) | | $2e + H^+$ | $\longrightarrow$ | e + H(n) | 67 |
| (50) | | $e + H_3^+$ + wall | $\xrightarrow{\gamma_{H_3^+}=1.0}$ | $H_2(X^1\Sigma_g^+) + H(1s)$ | |
| (51) | | $e + H_2^+$ + wall | $\xrightarrow{\gamma_{H_2^+}=1.0}$ | $H_2(X^1\Sigma_g^+)$ | |
| (52) | | $e + H^+$ + wall | $\xrightarrow{\gamma_{H^+}=1.0}$ | H(1s) | |
| (53) | Elec. detach. | $e + H^-$ | $\longrightarrow$ | 2e + H(1s) | 68 |
| (54) | Ion-ion | $H^- + H_3^+$ | $\longrightarrow$ | $2H_2(X^1\Sigma_g^+)$ | 67 |
| (55) | neutralization | $H^- + H_2^+$ | $\longrightarrow$ | $H_2(X^1\Sigma_g^+)$ + H(n>2s,2p) | 69 |
| (56) | | $H^- + H^+$ | $\longrightarrow$ | H(1s) + H(n=3) | 69 |
| (57) | Assoc. detach. | $H(1s) + H^-$ | $\longrightarrow$ | $e + H_2(X^1\Sigma_g^+)$ | 70 |
| (58) | Ion conversion | $H_2^+ + H_2$(v) | $\longrightarrow$ | $H_3^+ + H(1s)$ | 71–73 |
| (59) | | $H_2^+ + H(1s)$ | $\longrightarrow$ | $H^+ + H_2(X^1\Sigma_g^+)$ | 67 |
| (60) | | $H^+ + 2H_2$(v) | $\longrightarrow$ | $H_3^+ + H_2(X^1\Sigma_g^+)$ | 67 |
| (61) | | $H^+ + H_2$(v> 3) | $\longrightarrow$ | $H_2^+ + H(1s)$ | 67 |

$^\star$ Rate coefficient calculated by integrating the corresponding cross section over the eedf.

FIG. 1: Wall-recombination probability for the H atoms, as a function of the rf applied voltage, for the following pressures and frequencies: 0.3 torr (curves A and squares), 0.5 torr (curves B and circles), 1 torr (curves C and triangles); 13.56 MHz (solid lines and closed symbols), 27.12 MHz (dashed lines and crossed symbols), 40.68 MHz (dotted lines and open symbols). The points are the result of experimental in-situ measurements; the curves are fits to the experimental values, by using a power-law function $\gamma_{\rm H} = a(f,p)V_{\rm rf}^{b(f)}$.

FIG. 2: Axial profiles (at $r = 0$) of the time-average, steady-state charged particle densities, at $V_{\rm rf} = 200$ V, $f = 13.56$ MHz, and $p = 0.3$ torr. Results are for electrons (curve A); positive ions $H_3^+$ (B), $H_2^+$ (C) and $H^+$ (D); negative ions $H^-$ (E).

FIG. 3: Vibrational distribution function of hydrogen molecules at $p = 0.3$ torr, for $f = 13.56$ MHz (curves A) and 40.68 MHz (B), and for the following $V_{\rm rf}$ values: 50 V (solid curves); 100 V (dashed); 200 V (dotted).

FIG. 4: Time-average electron density (at $r = 0$ and $z = d/2$), as a function of the rf applied voltage, at $p = 0.3$ torr. The curves are simulation results, obtained with the complete kinetic of Tabs. I-III (solid curves) or using a simplified kinetic model for hydrogen[33] (dashed), at frequencies 13.56 MHz (curves A), 27.12 MHz (B), and 40.68 MHz (C). The points are experimental measurements, obtained using a planar probe (closed symbols) or a cylindrical Langmuir probe (open), at frequencies 13.56 MHz (squares), 27.12 MHz (circles), and 40.68 MHz (triangles). Simulations were multiplied by a factor of 3 for representation purposes.

FIG. 5: Effective electrical power coupled to the plasma, as a function of the rf applied voltage, at $p = 0.3$ torr. The curves (simulations) and the points (measurements) were obtained at frequencies 13.56 MHz (solid curves and squares), 27.12 MHz (dashed and circles), and 40.68 MHz (dotted and triangles).

FIG. 6: Electrical parameters as a function of $V_{\rm rf}$. **(a)** Time-average, steady-state plasma potential at $r = 0$ and $z = d/2$, $V_p(0, d/2)$; **(b)** Self-bias voltage, $V_{\rm dc}$. The curves and the points are for the same frequencies of Fig. 5.

FIG. 7: Time-average thickness of a mean space-charge sheath, as a function of the sheath voltage, at $p = 0.5$ torr. The curves (simulation results) and the points (semi-empirical results, obtained from electrical measurements) are for the same frequencies of Fig. 5.

FIG. 8: Time-average H atom density (at $r = 0$ and $z = 12$ mm), as a function of the rf applied voltage, at $p = 0.5$ torr. The curves (simulations) and the points (TALIF measurements) are for the same frequencies of Fig. 5. Simulations were multiplied by a factor of 4 for representation purposes. The insert in this figure plots the dissociation degree $n_{\rm H}/(n_{\rm H} + 2n_{\rm H_2})$ as a function of $V_{\rm rf}$ and for the same conditions.

FIG. 9: Effective electrical power coupled to the plasma, as a function of pressure, at $V_{\rm rf} = 100$ V. The curves (simulations) and the points (measurements) are for the same frequencies of Fig. 5.

FIG. 10: Time-average electron density (at $r = 0$ and $z = d/2$), as a function of pressure, at $V_{\rm rf} = 100$ V. The curves are simulation results, obtained with the complete kinetic of Tabs. I-III (solid curves) or using a simplified kinetic model for hydrogen[33] (dashed), at frequencies 13.56 MHz (curves A), 27.12 MHz (B), and 40.68 MHz (C). The points are experimental measurements, obtained using a Langmuir probe (closed symbols) or semi-empirically from electrical measurements (open), at frequencies 27.12 MHz (circles) and 40.68 MHz (triangles). Simulations were multiplied by a factor of 4 for representation purposes.

FIG. 11: Time-average H atom density (at $r = 0$ and $z = 12$ mm), as a function of pressure, at $W_{\text{eff}} = 30$ W. The curves are simulation results, obtained using $\gamma_{\text{H}}$ as shown in Fig. 1 (A) or $\gamma_{\text{H}} = 10^{-2}$ (B); the points are experimental TALIF measurements. Simulations (multiplied by a factor of 3 for representation purposes) and measurements are for the same frequencies of Fig. 5. The insert in this figure plots the dissociation degree $n_{\text{H}}/(n_{\text{H}} + 2n_{\text{H}_2})$ as a function of $p$ and for the same conditions.

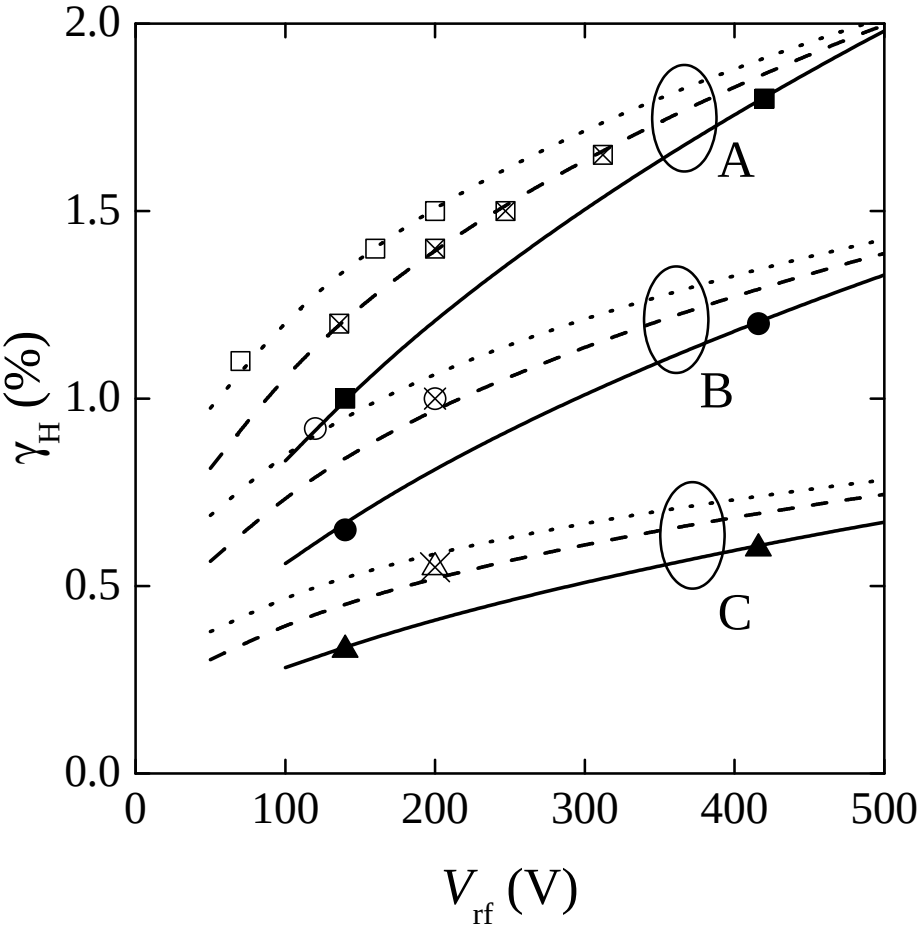


Fig.1

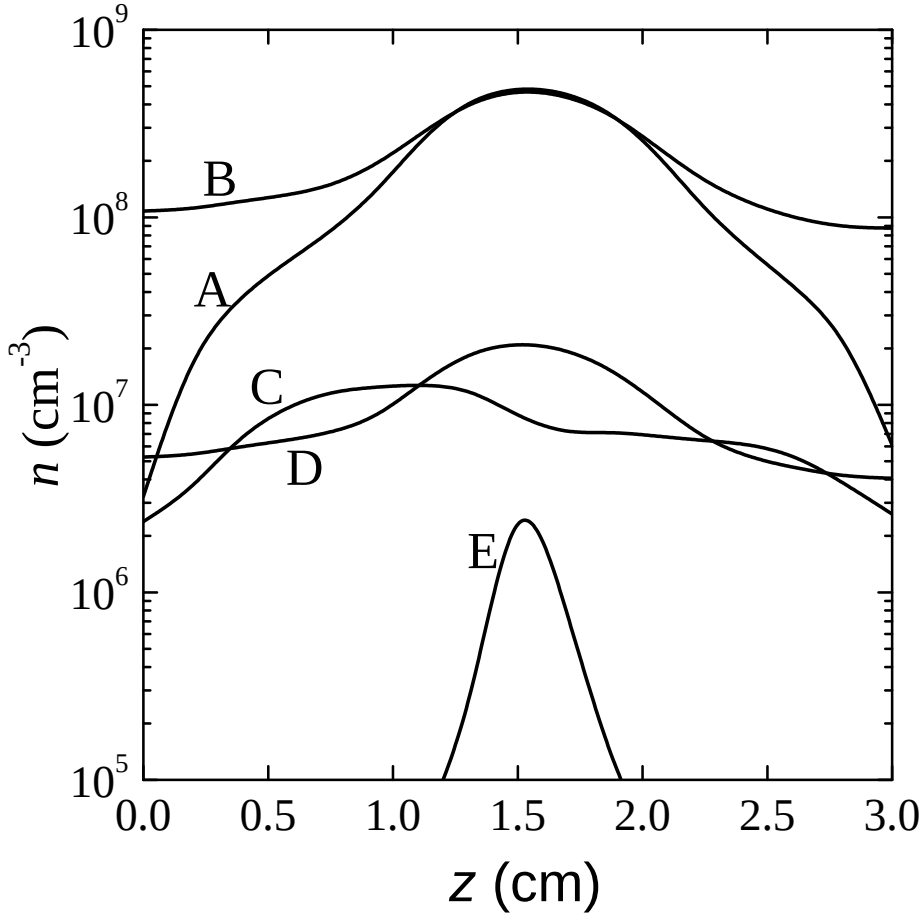


Fig.2

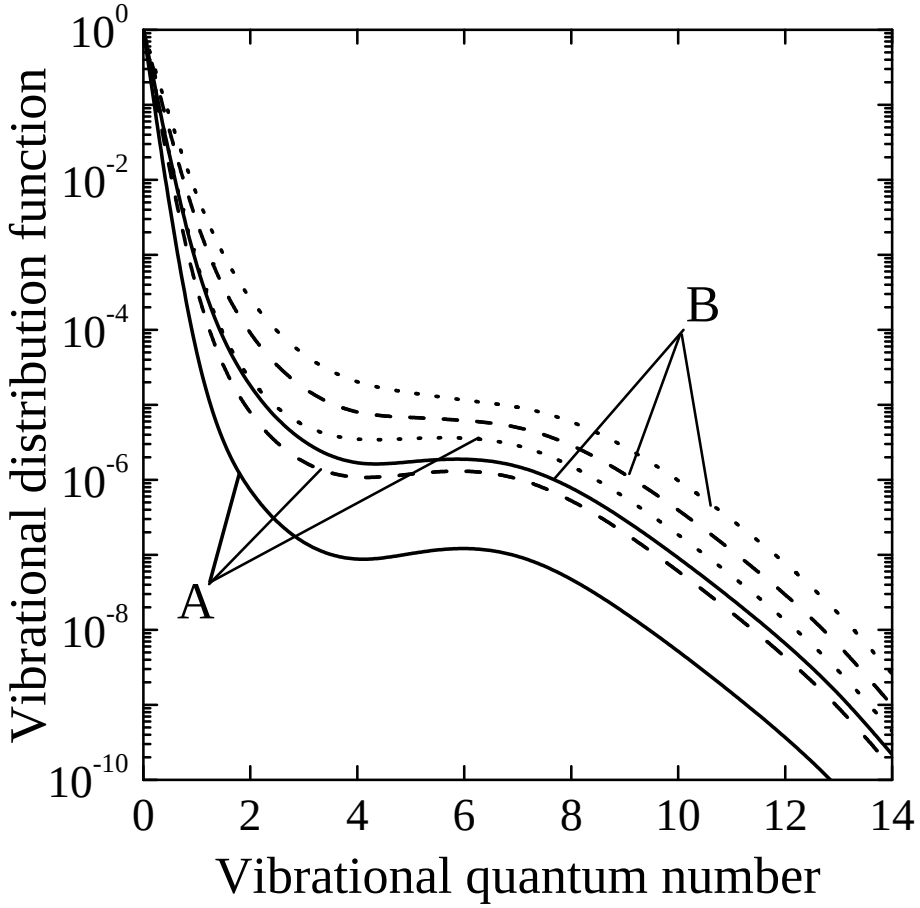
Vibrational distribution function
$10^{0}$
$10^{-2}$
$10^{-4}$
$10^{-6}$
$10^{-8}$
$10^{-10}$
0
2
4
6
8
10
12
14
Vibrational quantum number
A
B

Fig.3

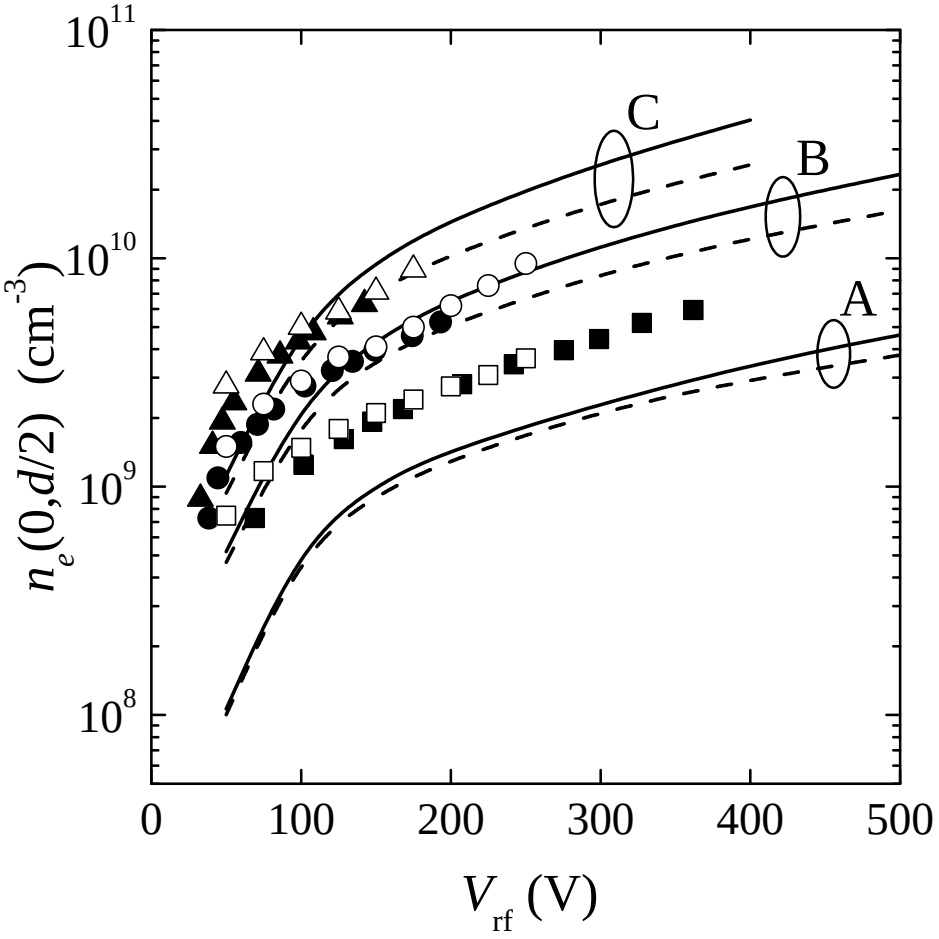


Fig.4

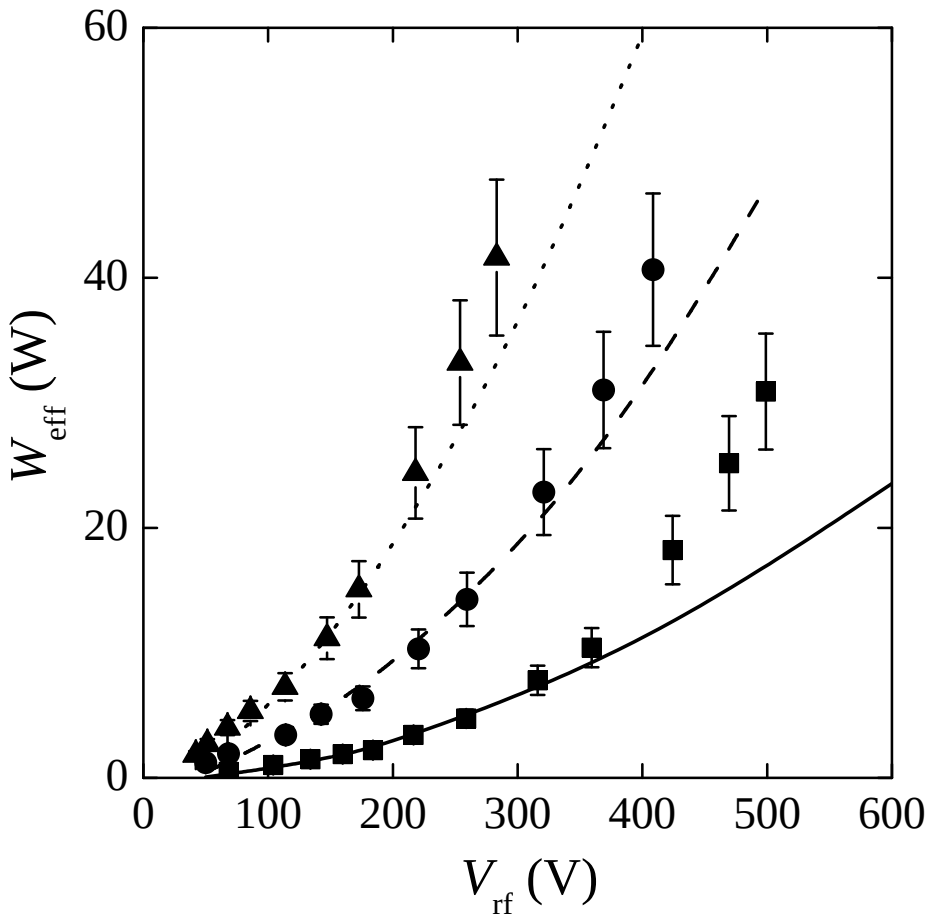


Fig.5

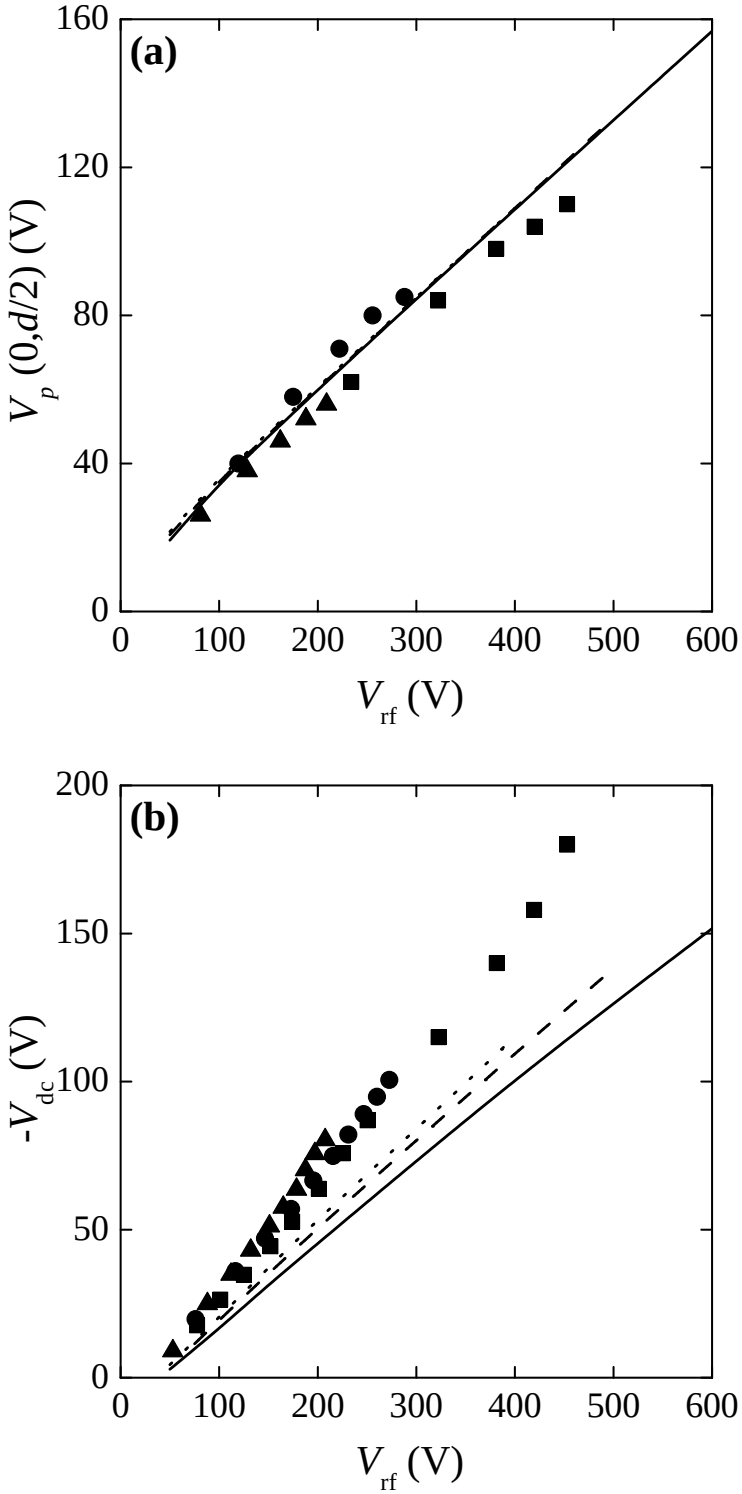
(a)
160
120
80
40
0
$V_p$ (0,$d$/2) (V)
0
100
200
300
400
500
600
$V_{rf}$ (V)
(b)
200
150
100
50
0
-$V_{dc}$ (V)
0
100
200
300
400
500
600
$V_{rf}$ (V)

Fig.6

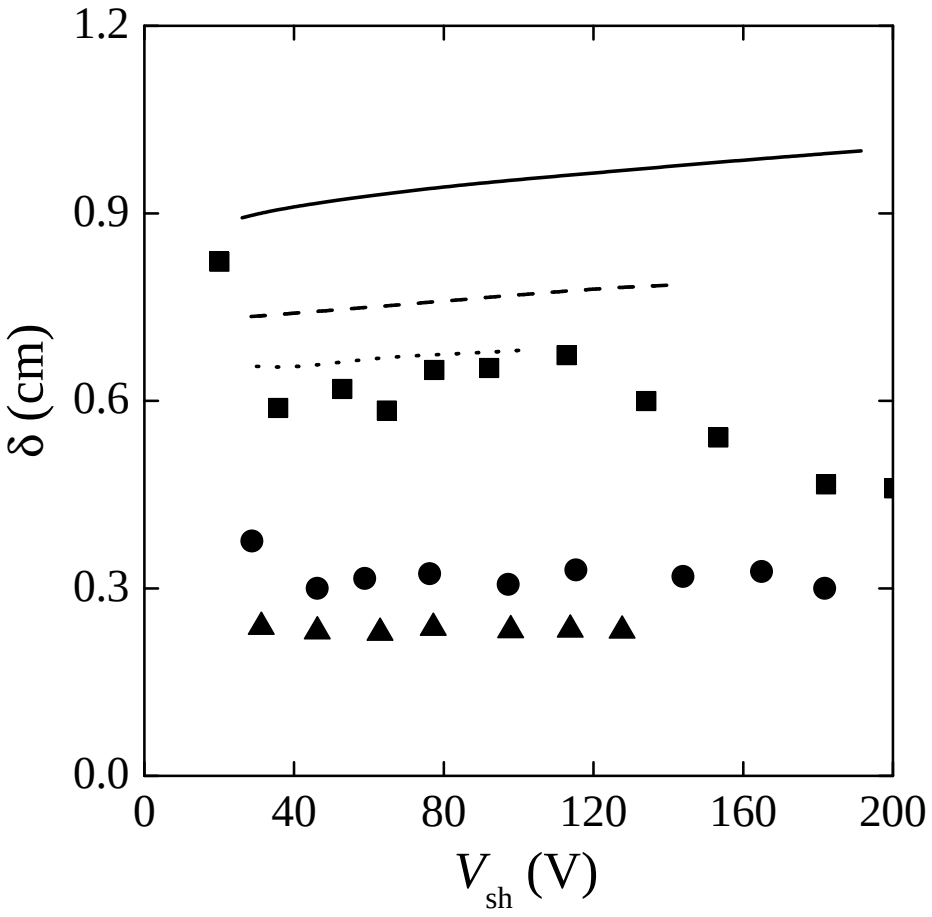


Fig.7

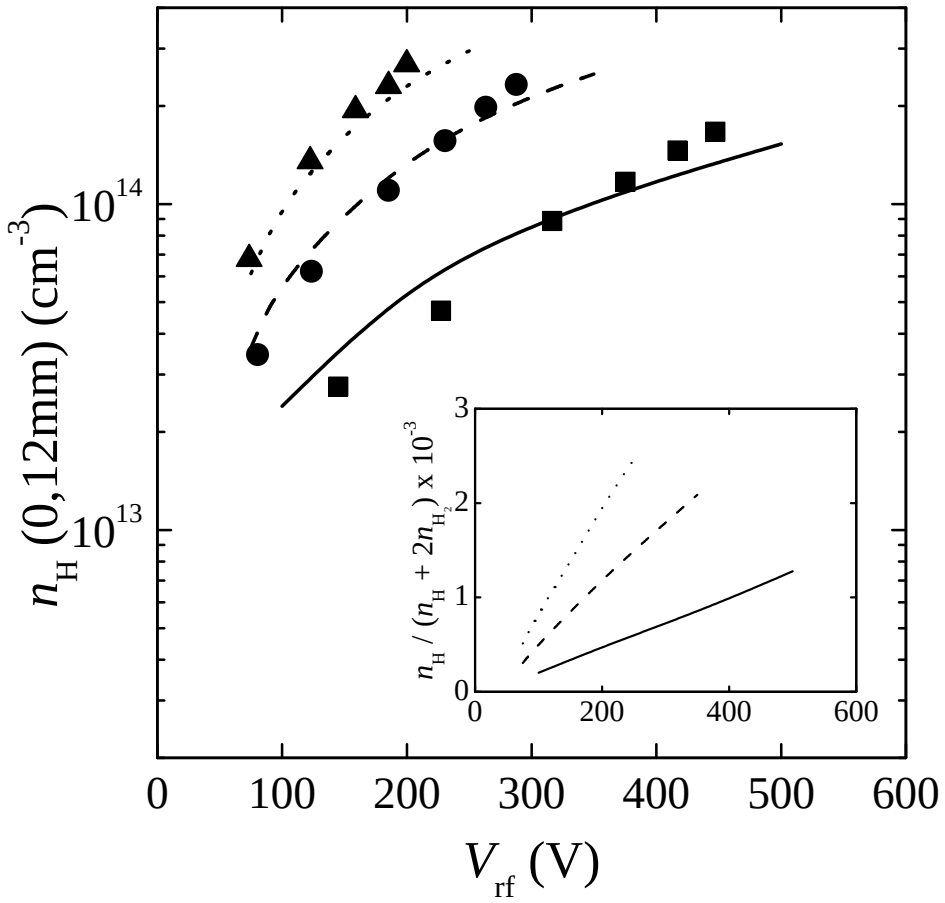
$n_H$ (0,12mm) (cm$^{-3}$)
$10^{14}$
$10^{13}$
0
100
200
300
400
500
600
$V_{rf}$ (V)
$n_H / (n_H + 2n_{H_2})$ x $10^{-3}$
3
2
1
0
0
200
400
600

Fig.8

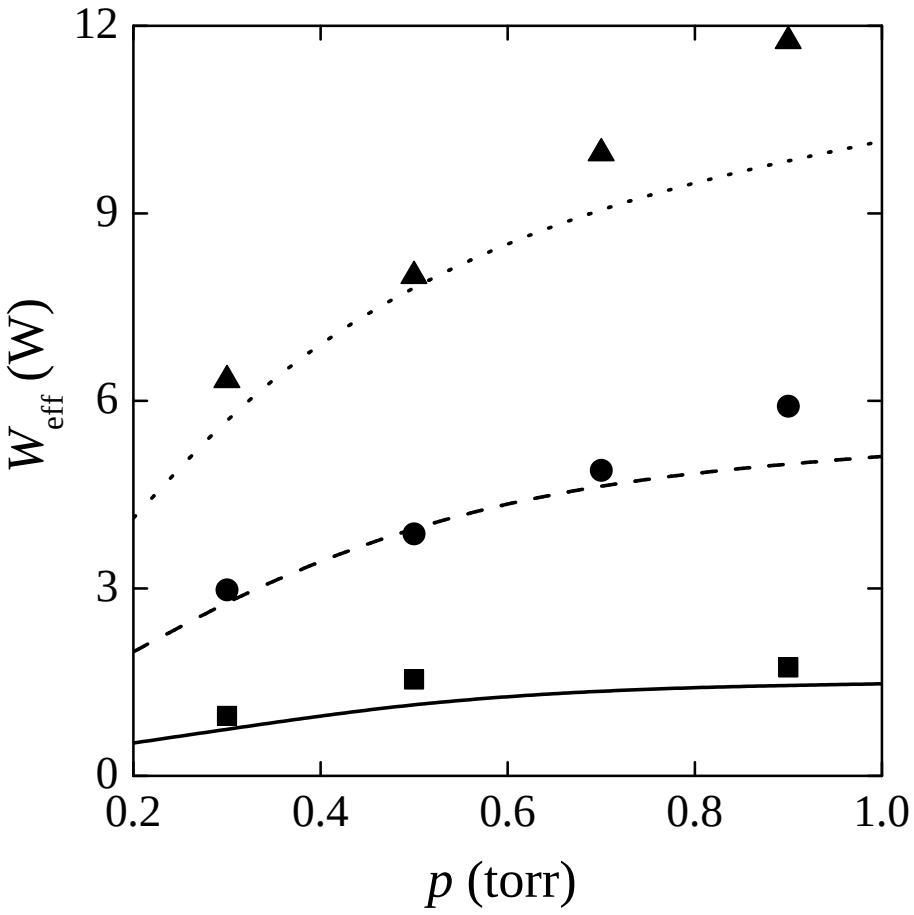


Fig.9

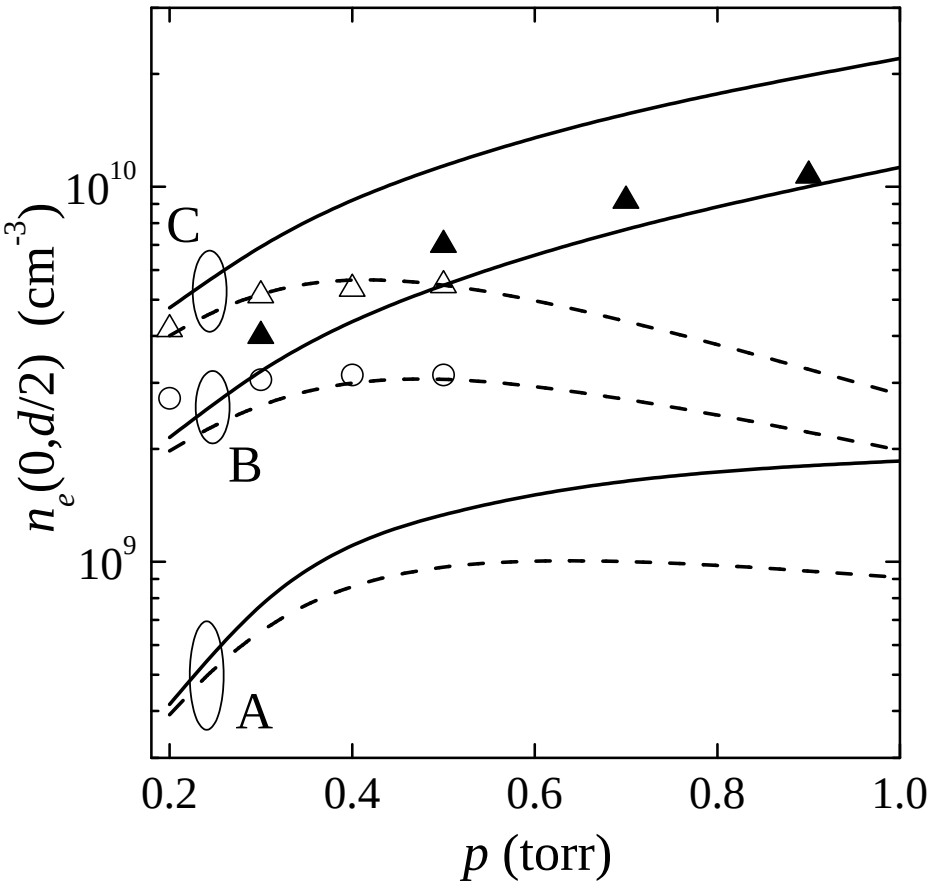


Fig.10

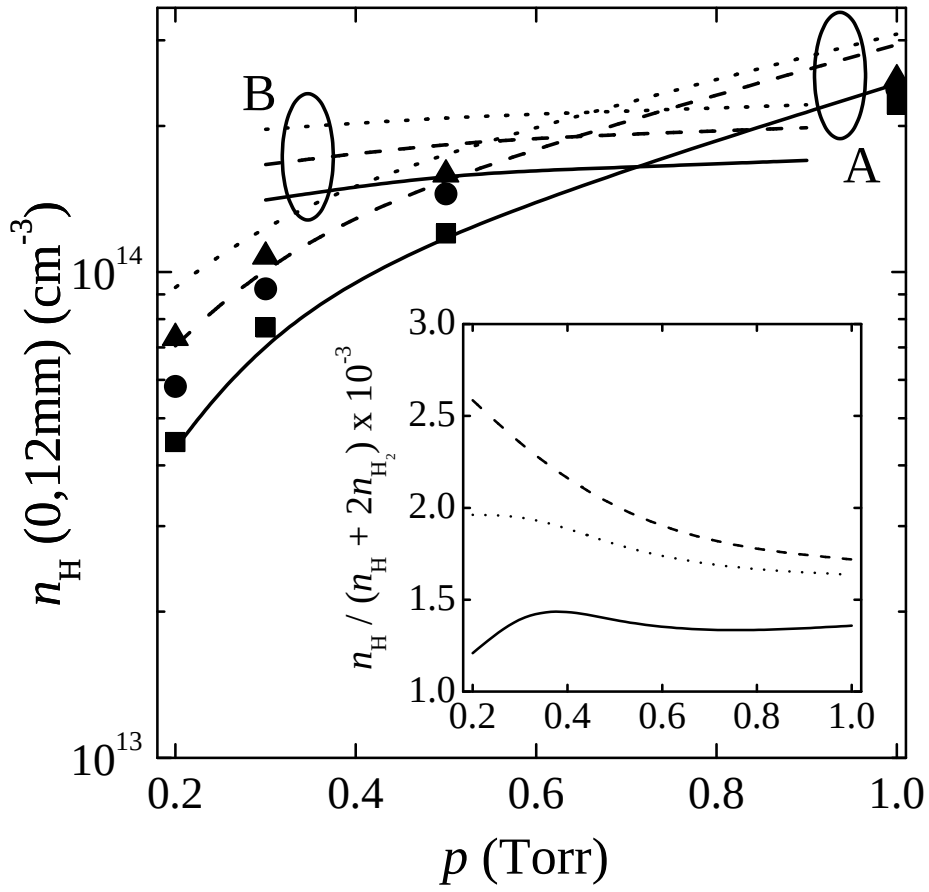
B
A
$n_H$ (0,12mm) (cm$^{-3}$)
$10^{14}$
$10^{13}$
0.2
0.4
0.6
0.8
1.0
$p$ (Torr)
$n_H / (n_H + 2n_{H_2})$ x $10^{-3}$
3.0
2.5
2.0
1.5
1.0
0.2
0.4
0.6
0.8
1.0

Fig.11